

## TURBULENT SWIRLING FLOW AND MIXING IN A MULTI-INLET VORTEX REACTOR

**Zhenping Liu**

Department of Mechanical Engineering  
Iowa State University  
Ames, IA USA  
payneliu@iastate.edu

**Emmanuel Hitimana**

Department of Mechanical Engineering  
Iowa State University  
Ames, IA USA  
hitimana@iastate.edu

**Michael G. Olsen**

Department of Mechanical Engineering  
Iowa State University  
Ames, IA USA  
mgolsen@iastate.edu

**James C. Hill**

Department of Chemical and Biological Engineering  
Iowa State University  
Ames, IA USA  
jchill@iastate.edu

**Rodney O. Fox**

Department of Chemical and Biological Engineering  
Iowa State University  
Ames, IA USA  
rofox@iastate.edu

### ABSTRACT

Turbulent swirling flow and mixing in a multi-inlet vortex reactor (MIVR) are of interest due to the importance of MIVR in flash nanoprecipitation applications. In current work, velocity and passive scalar concentration fields in a MIVR have been measured by using stereoscopic particle image velocimetry (SPIV) and planar laser induced fluorescence (PLIF). Measurements were taken at three different heights in the reactor. The measurements are focused near the reactor center where most of the intensive mixing happens. The investigated Reynolds numbers based on the bulk velocity and diameter at one of the reactor inlets range from 3290 to 8225, resulting in a complex turbulent swirling flow inside the reactor. The velocity and concentration field data were analyzed for such flow statistics as mean velocity, Reynolds stress, two-point spatial correlations of velocity fluctuations, scalar mean and variance, and one-point concentration probability density functions (PDF).

### INTRODUCTION

Functional nanoparticles are of great scientific and industrial interest for their unique size related properties and have a wide application in various areas, such as dyes, pesticides, and pharmaceuticals. However, it is challenging to produce functional nanoparticles in a relatively easy and inexpensive way. Flash NanoPrecipitation (FNP) has been developed to produce functional nanoparticles with a narrow particle size distribution (Johnson and Prud'homme, 2003). In the FNP technique, functional nanoparticles are formed by rapidly mixing supersaturated organic active and copolymer anti-solvent, resulting in organic active precipitation and particle growth where

the growing particle size of the organic active is frozen by deposition of block copolymer on its surface. Mixing time in the FNP technique should be short enough to provide a homogeneous starting time for the precipitation. Two mixer geometries, the Confined Impinging Jet Reactor (CIJR) (Liu et al. 2009) and the Multi-Inlet Vortex Reactor (MIVR) (Liu et al. 2008) have been developed to meet the high demand of rapid mixing in the FNP. While the CIJR is limited by the requirement of equal momenta of solvent and anti-solvent streams, the MIVR is insensitive to the equality of the momentum from each stream, allowing the final fluid phase to be anti-solvent dominant, which increases the stability of nanoparticles by depressing the rate of Ostwald Ripening. (Liu et al. 2008) Thus far, there have been many applications using the MIVR to produce functional nanoparticles.

In order to help understand the nanoprecipitation mechanism within the MIVR, mixing performance and flow characterization have been investigated in previous studies. Liu et al. (2008) evaluated the mixing performance of a micro-scale MIVR by using a competitive reaction and computational fluid dynamics (CFD). Cheng et al. (2009) measured flow velocity in the mixing chamber of a micro-scale MIVR by micro-PIV and compared the measurement with large eddy simulation. Shi et al. (2013) further presented detailed velocity measurements within the micro-scale MIVR to reveal the mean velocity field and turbulence characteristics. To study mixing and reaction, Cheng and Fox (2010) integrated a population balance equation with FNP kinetics into the CFD simulation. Their results show that the FNP process in the micro-scale MIVR is macro-mixing dominated, and the mixing is limited by the geometry of reactor, although increasing the Reynolds number can result in a more

homogeneous flow and improve the particle size distribution slightly. The laminar and turbulent mixing performance of the micro-scale MIVR was experimentally investigated by laser induced fluorescence with confocal laser scanning microscopy, and the mixing is found incomplete even at its highest investigated flow rate (Shi et al., 2011, 2014).

Despite the scalability of the MIVR in the FNP technique, most of previous research has focused on the micro-scale reactor (dimensions on the order of millimeters). While the micro-scale MIVR does show a great promise in the production of functional nanoparticles, some applications such as the use of nanoparticles in pesticides and cosmetics, require larger production runs than the micro-scale MIVR can provide. A scaled-up MIVR could potentially generate large quantities of functional nanoparticles in a both efficient and economical way. However, to the knowledge of the authors, there has been no research on scaling up the MIVR. In the current paper, the flow characteristics within a scaled-up MIVR (dimensions on the order of centimeters) are investigated for the first time using stereoscopic particle image velocimetry (SPIV) and planar laser-induced fluorescence (PLIF).

The scaled-up MIVR operates at a much higher Reynolds number than its micro-scale counterpart, resulting in a turbulent swirling flow in the mixing chamber. Although the configuration has not been studied before, some characteristics of the flow are similar to other swirling flows, and comparison with these swirling flows can enhance the understanding of the current investigation. Turbulent swirling flow exists in a wide range of fluid equipment such as cyclone separators, swirl combustors, engines with swirl inlets, etc. Swirling flow is known for the unsteady nature of its vortex center, which can be a random or precessing motion (Ingvorsen et al., 2013). In a turbulent swirling flow, the measured fluctuations can be enhanced by the vortex wandering motion which is called pseudo-fluctuation (Graftieaux et al., 2001). An inappropriate processing method for experimental data without considering the vortex wandering can smear the mean velocity field and exaggerate the turbulent fluctuations in the flow. Previous experimental work on the MIVR has not considered the influence of wandering motion on the calculated flow features. In the current paper, this influence is investigated extensively by comparing the results with and without considering the wandering motion, providing a better understanding of the flow turbulence inside the MIVR.

The flow inside the MIVR is highly three dimensional, especially close to the reactor center. This three-dimensional velocity field is investigated using stereoscopic particle image velocimetry (SPIV). SPIV employs two cameras to image the flow and extract all three components of flow velocity in a plane (Prasad, 2000). Based on the SPIV measurement, the flow characteristics in the macro-scale MIVR are analyzed extensively. The SPIV measurements are complemented by PLIF measurements of passive scalar mixing within the MIVR.

## EXPERIMENTAL METHODOLOGY

The experimental setup shown in Fig. 1 is designed to provide four independent inlet streams to the MIVR. The working fluid is water at room temperature. Each tank can contain a maximum of 1893 liters of liquid (500 Gallons). Flow from two feed tanks is powered by two pumps (*Mach pumps Inc.*) and sent to the four

inlets of the MIVR through four automatic control valves (*Fisher Inc.*). Each control valve provides a stable flow with accuracy around 0.5% for the investigated flow rate. Before the flow enters the reactor, the free stream turbulence intensity at each inlet of the MIVR is reduced by an 11 cm long flow conditioner containing 3.175 mm cell size honeycomb and screen grids. Flow exiting the reactor is pumped into two collection tanks and can be recycled back into the two feed tanks.

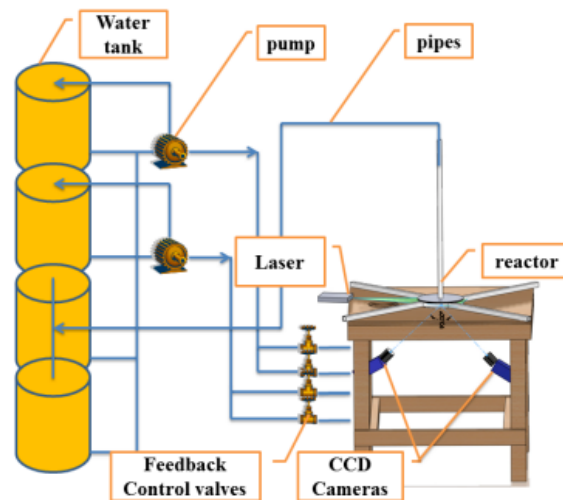


Figure 1. Schematic of the experimental setup

The macro-scale MIVR is made of acrylic glass to provide for good optical access. As shown in Fig. 2 (a) and (b), the reactor consists of four inlets, one outlet, and one mixing chamber. The four inlets are tangential to the mixing chamber in a 90 degree angular array. The outlet is located on the top center of the chamber. The cross section of the inlets are square in shape, 25.4 mm in width, and 870 mm in length. The cross section of the outlet is round with 25.4 mm diameter and 1067 mm length. The mixing chamber has a 25.4 mm height and 101.6 mm diameter. The dimensions of the macro-scale MIVR are about 16 times larger than those of the micro-scale reactor studied by Cheng et al. (2009) and Shi et al. (2013). However, due to different manufacturing methods, the macro-scale MIVR is similar yet not geometrically scaled up to its micro-counterpart.

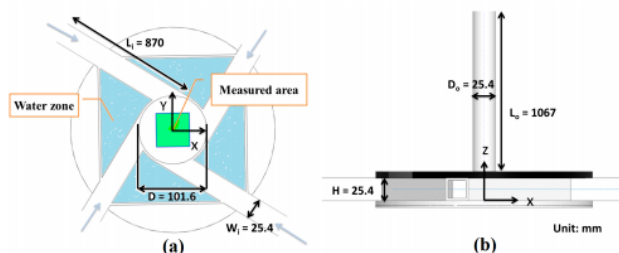


Figure 2: Geometry of the macro-scale MIVR. (a) Top view; (b) side view

There are two common ways of defining the Reynolds number for the MIVR. One way of defining Reynolds number is

based on one inlet and applied to the case where all four inlets have the same flow rate. The other type of Reynolds number is based on the diameter of mixing chamber which is used in the case where four inlets have different flow rates. In the current study, each inlet of the MIVR has been set up with the same flow rate, as previous studies have found the mixing performance to be insensitive to the inlet configuration (Liu et al., 2008). The investigated Reynolds number of the MIVR based on the bulk velocity of one inlet is  $3290 \sim 8225$ , corresponding to  $52640 \sim 131600$  when it is based on the mixing chamber. In the following sections, the Reynolds number  $Re_j$  is used, which is based on one inlet.

Stereoscopic particle image velocimetry was used to measure the velocity field inside the mixing chamber. The measured planes are located at the  $1/4$ ,  $1/2$ ,  $3/4$  and  $7/8$  height of the chamber along the  $z$ -direction. The  $1/8$  height was found difficult to measure because it is close to the bottom of the chamber, and there is a strong optical interference from seed particles depositing on the bottom. The flow was seeded with hollow glass spheres with diameter of  $11.7\mu\text{m}$  at a concentration of  $5.88\text{g}/\text{m}^3$ . The flow was illuminated by a double-pulsed Nd:Yag Laser (*New Wave Research Gemini*). The thickness of the laser sheet was  $1.5\text{ mm}$ . In order to minimize the refraction and reflection of the laser sheet on the curved surface of the chamber, four water filled zones were constructed around the chamber (Fig. 2 (a)). The time delay between the two laser pulses was chosen carefully so that average movement of particles was approximately  $5 \sim 8$  pixels, and out-of-plane particle motion was controlled to be less than 25% of the laser sheet thickness (Doorne and Westerweel, 2006). Two 12-bit double-frame CCD cameras (*LaVision Flowmaster 3S*) were used to capture the PIV images at a frequency of 8 Hz. The camera resolution was  $1280 \times 1024$  pixels with a pixel size of  $6.7\mu\text{m}$ . The viewing angle of the two cameras was set at nearly 90 degrees so that the measurement uncertainty in determining out-of-plane motions would be the same as in-plane motions. The accuracy of a stereoscopic PIV measurement relies on the implementation of a proper calibration. A general reconstruction technique based on a two-level calibration plate (*LaVision GmbH*) was applied here. This volumetric calibration method does not need facilities for moving the plate during calibration which is usually time-consuming and can easily introduce extra errors. The calibration grids use a high precision two-level dot pattern with  $2.2\text{ mm}$  dot diameter,  $10\text{ mm}$  dot spacing, and  $2\text{ mm}$  level separation. Due to the confined geometry of the MIVR, a mock reactor was used to hold the calibration plate, and an initial third-order mapping function was generated. After that, a self-calibration technique (Wieneke, 2005) was applied to correct the initial mapping function based on images taken for the real reactor to minimize the registration error which is found to play a dominant role in the accuracy of SPIV measurement. The area near the center of the reaction chamber was investigated (Fig. 2 (a)) rather than a plane covering the entire chamber because most of out-of-plane motion was found to occur near the center. For each Reynolds number 5000 image pairs were captured and analyzed by a commercial PIV software package Davis 7.2 (*LaVision GmbH*). A detailed introduction about stereoscopic PIV vector computation can be found in Callaud (2004). Multi-pass correlation techniques were used to compute vectors, resulting in a final interrogation

window size measuring  $32 \times 32$  pixels with 50% overlap, corresponding to a  $0.6\text{ mm}$  vector spacing. Although a smaller interrogation window such as  $16 \times 16$  pixels can provide more resolved information, it has an unacceptably high noise level.

As mentioned in the introduction, the average velocity field and turbulence statistics can be affected by the wandering motion of the vortex center. It is therefore important to track the wandering motion of the vortex center before choosing an appropriate processing method. For the flow in the MIVR, a single vortex center is observed for all realizations. The center of mass approach proposed by Ingvorsen et al. (2013) is adopted here to identify the vortex center. In detail, the function  $W$ , *i.e.*, the magnitude of axial vorticity  $W_z$  divided by in-plane velocity magnitude is calculated, and this should have its maximum value at the vortex center. The vortex center  $R$  is computed as the center of mass of all positions with  $W_z$  larger than 0.95 of the maximum  $W$ . The position of the vortex center is calculated for 5000 instantaneous velocity fields. The wandering range of the vortex center is found to be similar for all measurement planes. Using the measured locations of the instantaneous vortex center, two methods are applied here to investigate the effect of wandering motion on the ensemble-averaged velocity, TKE, and Reynolds stress. The first method (referred to as Method One) is to calculate these statistical features in a fixed frame centered at the geometric center of the reactor. In the second method (referred to as Method Two), each instantaneous result is transformed to a new frame where its vortex center is set as the origin. Statistical features are then determined based on the new set of 5000 instantaneous fields.

In the planar laser-induced fluorescence experiments, the working fluid is deionized water at room temperature. Flow from two supply tanks is pumped into the four inlets of the MIVR where the flow rate can be adjusted using four automatic control valves (*Fisher Inc.*). The flow in the chamber of the MIVR is illuminated by a Nd:YAG laser with a laser-sheet thickness of  $1\text{ mm}$ . One 12-bit CCD camera (*LaVision Imager Intense*) was used to capture images at a frequency of 8 Hz through the bottom of the MIVR. A long-pass optical filter that blocked light with wavelength shorter than  $542\text{ nm}$  was mounted in the camera lens so that reflected and scattered laser light did not interfere with the fluorescence measurement.

The fluorescent dye Rhodamine 6G was used as the passive scalar. Two inlets were fed with water while the other two were fed with water containing Rhodamine 6G with a concentration of  $45\mu\text{g}/\text{L}$ . The concentration level of Rhodamine 6G was carefully selected so that the local intensity of the fluorescent light was proportional to the local intensity of the excitation source and the local concentration of the fluorescent dye. The shot-to-shot variation of the laser power was found to be approximately 2%. Thus, it was not necessary to calibrate the PLIF images based on the shot-to-shot laser power variation. Each PLIF image was calibrated to eliminate the non-uniform energy distribution of laser sheet based on the procedure described by Feng et al. (2005). The three PLIF measurement planes were located at the  $1/4$ ,  $1/2$  and  $3/4$  height of the chamber along the  $z$ -direction. The investigated Reynolds number is defined based on the bulk velocity of one inlet, as all four inlets have the same flow rate. Four Reynolds numbers were investigated in the experiment

ranging from 3290 to 8225. For each case, 5000 instantaneous PLIF images were captured for analysis.

**RESULTS AND DISCUSSION**

Figure 3 shows example instantaneous and ensemble-averaged SPIV measurement results at all four measured planes for a Reynolds number of 3290. It can be seen that the instantaneous velocity shown in the left hand figure shows irregularities compared to the smooth streamlines in the right hand figure for the averaged velocity, indicating that flow has already become turbulent at  $Re = 3290$ . The streamlines in all the velocity fields reveal that flow undergoes a spiral motion towards the center and a single vortex center is observed for all measurement planes. The pattern is clearer in the ensemble-averaged velocity fields. Far away from the vortex center, streamlines show that flow approaches the center through the spiral motion. Near the vortex center, the streamlines resemble concentric circles, indicating that the core-region is similar to a potential vortex where radial velocity becomes negligible

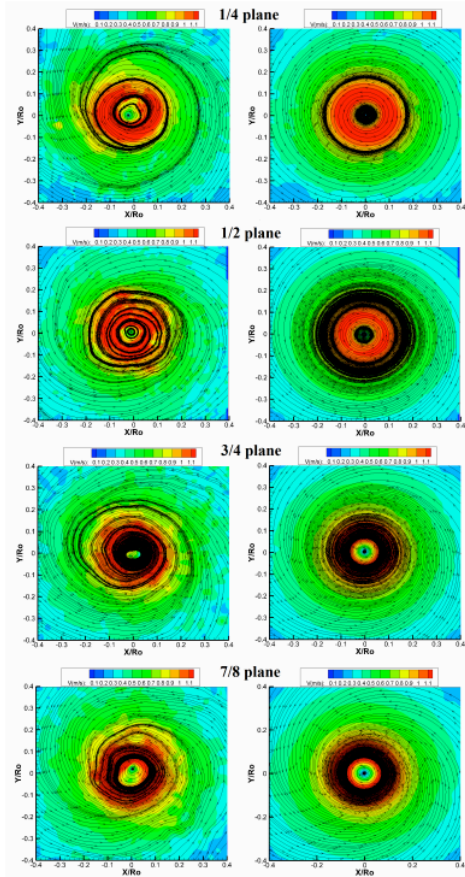


Figure 3. Typical instantaneous velocity fields at the four measurement planes (left) and corresponding ensemble-averaged velocity (right) for  $Re=3290$ . The magnitude of velocity is indicated by the colored contour. The solid lines are streamlines based on in-plane velocities.

Ensemble-averaged velocity is obtained using both Method One and Method Two previously introduced in the Post

processing section. To compare average velocity in different measurement planes, the radial, azimuthal, and axial velocity profiles are extracted from the SPIV measurements using the averaging method mentioned in the Post-processing section. These three velocities are then normalized by the bulk inlet velocity  $U_j$ . It is found that none of the ensemble-averaged velocities display any significant change between the use of Method One or Method Two. This finding reveals that the wandering motion of vortex center has little effect on the ensemble-averaged velocity, which is consistent with the finding in Ingvorsen et al. (2013) that ensemble-averaged velocity profiles of swirling flow obtained at a fixed frame could well represent the key flow features for a small wandering motion.

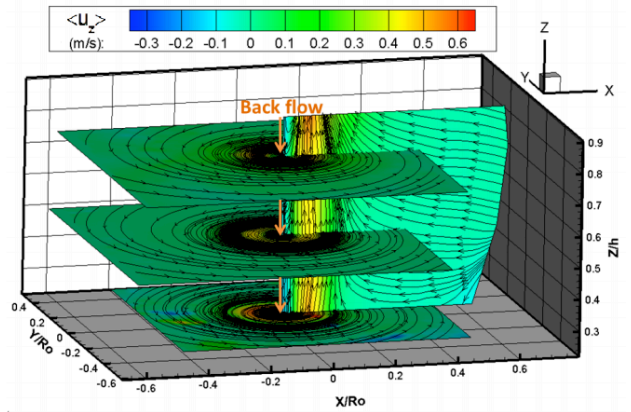


Figure 4. Mean flow pattern when  $Re=3290$ . The axial velocity is shown by the contour plot.

A visualization of the mean flow pattern in the mixing chamber of the MIVR can be obtained by putting all the measured planes in a three-dimensional coordinate, as shown in Fig. 4. Due to optical access constraints, the X-Z plane shown in Fig. 4 has not been measured. Instead, it is constructed based on the information from X-Y planes. In practice, the velocity at four intersection lines between the X-Z plane and the measured plane, i.e., the X-Y plane, can be obtained from the SPIV measurements at the 1/4, 1/2, 3/4 and 7/8 planes. Based on the measured velocities for these four planes, the velocity field in the X-Z plane has been constructed. Streamlines in the X-Y plane show that the flow moves toward the center in a spiral motion. Streamlines in the X-Z plane reveal how flow from the horizontal inlets comes to the vertical outlet. In detail, flow from the inlet first slowly moves towards the center and then accelerates as it escapes from the chamber. It can be seen that there is a small region of back flow in the vortex center. Most of the out-of-plane motion happens near the center area, and it is found that part of the back flow is reverted towards the exit by the outflow. The vortex flow is stabilized by the inlet momentum and centrifugal force, producing a pear shape of streamlines near the center at X-Z plane where flow goes outwards near the 1/4 plane and then inwards near the 3/4 and the 7/8 planes.

Turbulent kinetic energy (TKE) is calculated using the measured root-mean-square velocity fluctuations. It is important to provide correct measured TKE as a reference for computational work. However, for flow in the MIVR, the measured TKE can be affected by the vortex wandering, resulting

in a much higher measured TKE than the real turbulent fluctuation. That is because the instantaneous velocity near the center can be significantly changed by the vortex wandering. This change, referred to as pseudo-fluctuation, is more like a structure motion than a turbulent fluctuation and is due to the instantaneous unequal momenta of inlet flow (Graftieaux, 2001) This pseudo-fluctuation can contaminate the measured TKE in swirling flow, making it difficult to know the real turbulence strength inside the flow.

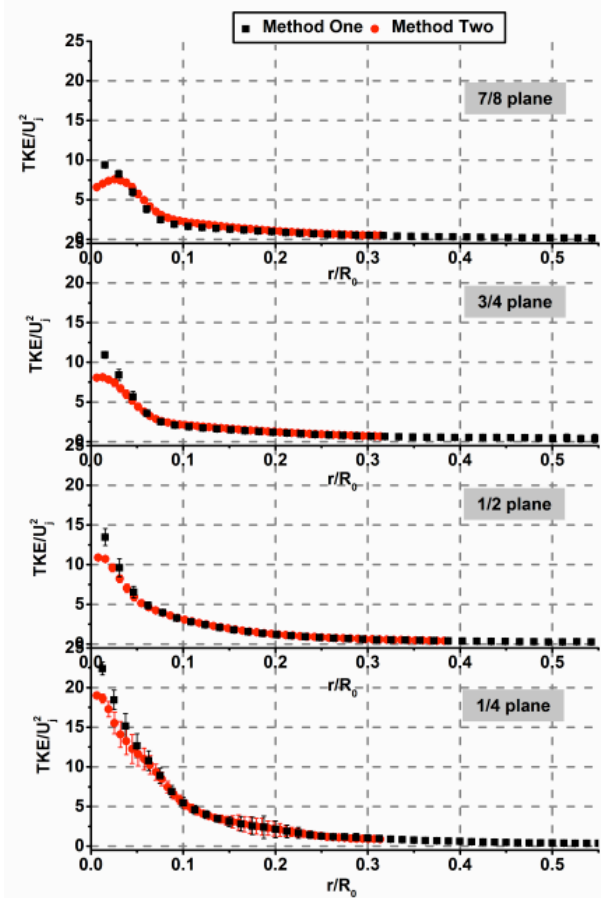


Figure 5. Comparison of normalized TKE by Method One and Method Two when  $Re=3290$ .

To investigate the influence of the pseudo-fluctuation on the measured TKE, Method One and Method Two are adopted here to calculate the TKE at all four measurement planes. The TKE is normalized by  $U_j^2$ . For both results, the TKE contours is found to be nearly axisymmetric in the measured plane and are presented in Fig. 5. The TKE calculated by the two methods is found to be almost the same when dimensionless radius  $r/R_0$  is larger than 0.05, indicating that vortex wandering only affects the TKE in a small region near the center. When  $r/R_0$  is smaller than 0.05, the TKE calculated by Method Two becomes smaller than that by Method One. This is because the wandering motion of the vortex center is eliminated by Method Two. The reduced percentage of the maximum TKE ranges from 17% to 30% for all four measurement planes. This finding shows that calculating the TKE without considering the vortex wandering

will overestimate its value by up to 30%. The TKE by both methods begins to decrease with increasing plane height. For example, the maximum normalized TKE at the 1/4 plane is calculated to be 19 by Method Two, while it decreases to 7.57 at the 7/8 plane. It can be seen that TKE far away from the vortex center is quite small compared to that in the center. As the flow approaches the center, the TKE increases significantly. This non-uniform distribution of TKE suggests that most turbulent mixing happens near the center area where velocity fluctuations are strong.

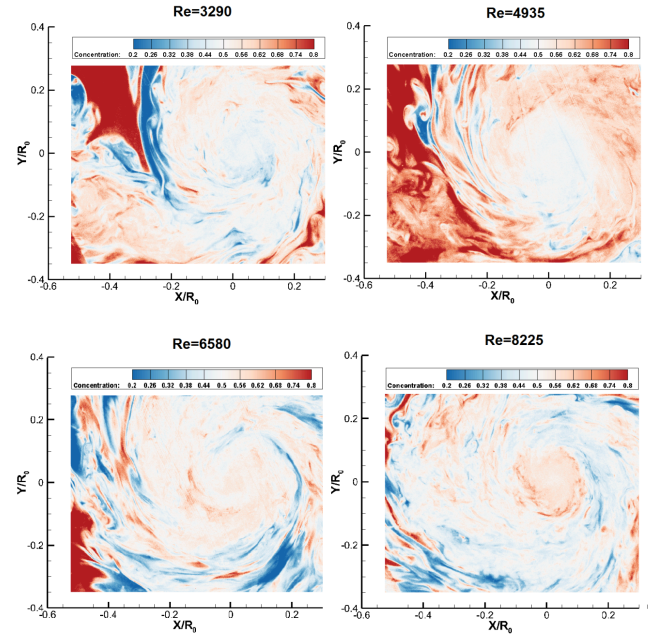


Figure 6. Typical instantaneous passive scalar field for  $\frac{1}{2}$  plane at different Reynolds numbers.

The mean velocity of turbulent swirling flow in the MIVR can be described using a Batchelor Vortex Model (Liu et al, 2014)

$$\bar{u}_\theta(r) = \frac{V_1 R_1^2}{r} \left[ 1 - \exp\left(-\frac{r^2}{R_1^2}\right) \right] + \frac{V_2 R_2^2}{r} \left[ 1 - \exp\left(-\frac{r^2}{R_2^2}\right) \right] \quad (1)$$

$$\bar{u}_z(r) = U_0 + U_1 \exp\left(-\frac{r^2}{R_1^2}\right) + U_2 \exp\left(-\frac{r^2}{R_2^2}\right) \quad (2)$$

where the model can be viewed as the combination of two Batchelor Vortices.  $R_1$ ,  $V_1$ , and  $U_1$  are the characteristic values of one vortex, and  $R_2$ ,  $V_2$ , and  $U_2$  are for the other vortex.  $U_0$  depends on the inlet flow rate and  $U_1$ ,  $U_2$ ,  $R_1$ , and  $R_2$ . Based on the mean velocity fields, the turbulent swirling flow in the MIVR can be divided into two regions, i.e., a free-vortex region ( $r/R_0 > 0.2$ ) and a forced-vortex region ( $r/R_0 < 0.1$ ) where  $R_0$  is the radius of MIVR chamber and  $r$  is the distance from the reactor center. The region for  $0.1 < r/R_0 < 0.2$  is the transitional area between the forced-vortex and free vortex region. The turbulence intensity in the forced-vortex region is much higher than in the free-vortex region (Liu et al., 2015). As passive scalar transport is strongly

dependent on the turbulence field, it is natural to describe the scalar field separately in these two regions.

Figure 6 shows typical results for the instantaneous passive scalar from the  $\frac{1}{2}$  plane where several interesting features can be identified. First, a large-scale vortical structure can be identified in the scalar field within which fluid of different concentrations mixes spirally in the free-vortex region, while an almost homogeneous scalar field without apparent unmixed regions forms in the forced-vortex region. It is observed that unmixed fluid is stretched into thin layers as the flow spirals towards the reactor center and some of these layers preserve their shape well until they enter the forced-vortex zone. As the Reynolds number increases, the local unmixed region in the free-vortex region is reduced from large bulk shapes at  $Re=3290$  to thin-strip shapes at  $Re = 8225$ . It is expected that the size of the local unmixed scalar in the free-vortex region could be further reduced at even higher Reynolds number. As would be expected, the instantaneous scalar field clearly shows that the swirling flow has a much better mixing performance in the forced-vortex region than in the free-vortex region. The passive scalar is expected to be well mixed as it approaches the reactor outlet located in the forced-vortex region. Both the turbulence field and the vortex wandering motion contribute to the enhanced mixing in the forced-vortex region.

## CONCLUSIONS

An experimental investigation was performed to quantify the turbulent swirling flow within a scaled-up multi-inlet vortex reactor (MIVR). The flow characteristics were investigated using stereoscopic particle image velocimetry (SPIV) and planar laser-induced fluorescence (PLIF). Various measurement planes in the mixing chamber were investigated for Reynolds numbers ranging from 3290 to 8225. The influence of vortex wandering on the mean velocity field and turbulence characteristics was assessed by using two different processing methods. Method One, which calculates velocity statistics in a fixed frame, was used as a control group for Method Two, where the vortex wandering was eliminated by keeping the instantaneous vortex center at the coordinate origin. Reynolds number effects were investigated by comparing flow characteristics at different Reynolds numbers. The main findings of the current work are as follows:

1. Turbulent swirling flow in the MIVR is unstable with its vortex center wandering in a small region whose diameter is about 5% of the chamber.
2. The measured TKE and Reynolds stress are sensitive to the wandering of the vortex center. The maximum value of TKE calculated by Method Two is reduced by 17% to 30% at all four measurement planes compared to that by Method One.
3. A recirculating back flow exists at the center of the reactor.
4. The mean velocity is accurately described by a Batchelor Vortex Model.

## REFERENCES

Calluaud, D., 2004. Stereoscopic particle image velocimetry measurements of the flow around a surface-mounted block. *Exp Fluids*, Vol. 36, pp. 53–61.

Cheng, J. C.; Fox, R. O. 2010. Kinetic modeling of nanoprecipitation using CFD coupled with a population balance. *Ind. Eng. Chem. Res.* Vol. 49, pp. 10651–10662.

Cheng, J. C., Olsen, M. G., Fox, R. O., 2009. A microscale multi-inlet vortex nanoprecipitation reactor: Turbulence measurement and simulation. *Appl. Phys. Lett.* Vol. 94, 204104.

Doorne, C. W. H., Westerweel, J., 2006. Measurement of laminar, transitional and turbulent pipe flow using Stereoscopic-PIV. *Exp Fluids*, Vol. 42, pp. 259–279.

Feng, H., Olsen, M.G., Liu, Y., Fox, R.O., Hill, J.C., 2005. Investigation of turbulent mixing in a confined planar-jet reactor. *AIChE J.*, Vol. 51, pp. 2649–2664.

Graftieaux, L., Michard, M., Grosjean, N., 2001. Combining PIV, POD and vortex identification algorithms for the study of unsteady turbulent swirling flows. *Meas. Sci. Technol.* Vol. 12, pp. 1422–1429.

Ingvorsen, K. M., Meyer, K. E., Walther, J. H., Mayer, S., 2013. Turbulent swirling flow in a model of a uniflow-scavenged two-stroke engine. *Exp Fluids*, Vol. 54, 1494.

Johnson, B. K.; Prud'homme, R. K. 2003. Flash nanoprecipitation of organic actives and block copolymers using a confined impinging jets mixer. *Aust. J. Chem.* Vol. 56, pp. 1021–1024.

Liu, Y., Cheng, C., Prudhomme, R. K., Fox, R. O. 2008. Mixing in a multi-inlet vortex mixer (MIVM) for flash nanoprecipitation. *Chem. Eng. Sci.* Vol. 63, pp. 2829–2842.

Liu, Y., Olsen, M. G., Fox, R.O. 2009. Turbulence in a microscale planar confined impinging jets reactor. *Lab Chip*, Vol. 9, pp. 1110–1117.

Liu, Z., Fox, R.O., Hill, J.C., Olsen, M.G., 2014. A Batchelor vortex model for mean velocity of turbulent swirling flow in a macroscale multi-inlet vortex reactor. *J. Fluids Eng.*, Vol. 137, 041204.

Liu, Z., Ramezani, M., Fox, R.O., Hill, J.C., Olsen, M.G., 2015. Flow characteristics in a scaled-up multi-inlet vortex nanoprecipitation reactor. *Ind. Eng. Chem. Res.*, Vol. 54, pp. 4512–4525.

Prasad, A. K., 2000. Stereoscopic particle image velocimetry. *Exp Fluids*, Vol. 29, pp. 103–116.

Shi, Y., Cheng, J. C., Fox, R. O., Olsen, M. G. 2013. Measurements of turbulence in a microscale multi-inlet vortex nanoprecipitation reactor. *J. Micromech. Microeng.* Vol. 23, 075005.

Shi, Y., Fox, R. O., Olsen, M. G., 2011. Confocal imaging of laminar and turbulent mixing in a microscale multi-inlet vortex nanoprecipitation reactor. *Appl. Phys. Lett.*, Vol. 99, 204103.

Shi, Y., Fox, R. O., Olsen, M. G., 2014. Micromixing visualization and quantification in a microscale multi-inlet vortex nanoprecipitation reactor using confocal-based reactive micro laser-induced fluorescence. *Biomicrofluidics*, Vol. 8, 044102.

Wieneke, B., 2005. Stereo-PIV using self-calibration on particle images. *Exp Fluids*, Vol. 39, pp. 267–280.